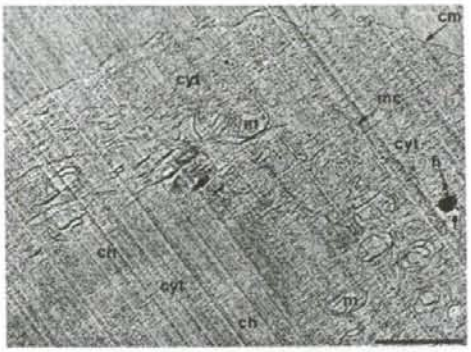


**Fig. 1.** Cryo-EM view of a vitreous section of a mitotic HeLa S3 cell. Chromosomes are recognized by their elongated aspect and uniform texture. Numerous granules, membrane cisterns (mc), vesicles, and mitochondria (m) are evident in the cytoplasm, which is bordered by the cytoplasmic membrane (cm). Oblique striations of the image intensity are the result of knife marks during the sectioning process. A surface contamination with hexagonal ice (h) is also seen. The section thickness is ~60 nm. (Scale bar, 1 μm.)

in segregation of the compact structure of the native chromosome into 30-nm fibers.

## Results

**The Uniform Homogeneous Grainy Texture of Chromosome Images Is Maintained After CTF Correction.** The general appearance of a vitreous section of a mitotic HeLa S3 cell is shown in Fig. 1. The cytoplasm contains grains and various membranous organelles, such as cisterns of the endoplasmic reticulum and mitochondria. The homogeneous domains in the central region of the cell, excluding the globular macromolecular complexes and membranes, are chromosomes.

The homogeneous grainy texture enables the identification of the HeLa S3 chromosomes at a higher magnification (Fig. 2*A*, raw image). The figure shows 3 regions of condensed chromosomes separated by a thin branched zone of cytoplasm, which is recognizable by the presence of numerous globular macromolecular complexes. The chromosomes are well delineated, with smooth surfaces that are devoid of complicated convolutions. In addition, the characteristic homogenous grainy texture of the chromosomes becomes better visible at this magnification (25,500×).

The image was taken with an objective lens that was defocused at 6.6 μm, to generate sufficient phase contrast. Consequently, this image, as with any phase-contrast TEM image, is affected by the CTF. The CTF results in artificial amplification or suppression of the signal intensity, which, depending on the defocus value, affects different structural features. Although this effect is not easy to discern in the real-space image, it is evident in its computed diffraction pattern. Because the macromolecules are arbitrarily oriented within the sample, for general evaluation the diffraction pattern presented as a power spectrum can be rotationally averaged. The resulting graph [rotationally averaged power spectrum (1-DRAPS)] plots the averaged amplitudes on the *y* axis and the spacings on the *x* axis.

The 1-DRAPS of the entire image (Fig. 2*A*, raw image) had the highest signal peak at ≈11-nm spacing, indicating that structural features of this size predominate. However, because of CTF, the average amplitude dropped dramatically for the 30-nm spacing, which might have resulted in putative 30-nm fibers being hidden.

To compensate for the signal distortions caused by the CTF, several images of the same area were taken at different defocusing values and merged into a single image. This technique is used routinely with single particle cryo-EM to minimize the effects of CTF (24). In the present study, we applied this technique to search more sensitively for any possible higher-order chromatin structure. This type of deconvoluted focal series reconstruction (Fig. 2*A*, CTF-corrected image) combines the information from 5 images of a mitotic HeLa S3 cell taken at defocus values of between 6.6 and 26.8 μm. The recovery of the 30-nm features was apparent in the 1-DRAPS as a rise of average amplitude for the 30-nm spacing (Fig. 2*A*, 1-DRAPS of CTF-corrected image). Consistently, the 30-nm features of the cytoplasm, which were faint in the raw image, including globular macromolecular complexes [which most probably correspond to ribosomes (arrows), because of their dimensions], were clearly visible in the reconstructed image (Fig. 2*A*, CTF-corrected image).

However, no structures of this size were discernible in the chromosomes. The CTF-corrected grainy pattern of the chromosome image consisted of dense dots, which had a next-neighbor distance, directly estimated in the image, of 10–15 nm. The same CTF-correction procedure was performed for other 4 areas of the size of Fig. 2, which were randomly picked in different mitotic HeLa S3 cells. We found no difference in the CTF-corrected texture of chromosomes between the cells. The images did not reveal any obvious higher-order arrangement of the grains. The grainy pattern was essentially homogenous; there were no characteristic grain arrangements extending over distances significantly longer than 15 nm (Fig. 2*B*).

Because the images in Fig. 2*A* represent projections of a section of ≈50-nm thickness, which is much thicker than the size of a single nucleosome (≈10-nm diameter and 6-nm thickness), the grains seen in the image are superimpositions of perhaps 4–8 nucleosomes. If these nucleosomes were to be arranged in a regular order, some favorable orientations would reveal characteristic patterns in the images. For example, top views of 30-nm chromatin filaments of a length similar to our section thickness, modeled on the basis of in vitro observations (22), would give rise to characteristic rosette patterns (Fig. 2*B Inset*). The volume of such a chromatin patch (≈40,000 $nm^3$) corresponds to 1/1000 of the chromatin volume of the section presented in Fig. 2. Given that chromosomes consist of randomly oriented 30-nm filaments, it provides a good chance for 30-nm fibers, if they exist, to be imaged as the characteristic top views. However, these or other ordered patterns were never observed in the condensed chromosomes; we found no authentic 30-nm filaments regularly arranged over a dimension of the order of the section thickness in this or any other section that we viewed (Fig. 2*B*).

**Quantitative Analysis by 1-DRAPS Reveals Characteristic Spacing Peaks that Distinguish Textures of Chromosomes and Cytoplasm.** To quantitatively analyze the chromosome texture, we obtained 1-DRAPS selectively for chromosomal and cytoplasmic areas over a number of images. These spectra were CTF-corrected and averaged into 1 graph to improve the signal-to-noise ratio [for details, see *Materials and Methods* and supporting information (SI) *Text* and Fig. S1].

The resulting 1-DRAPS images are shown in Fig. 3. A broad peak of spacing with a maximum of ≈11.3 nm was observed for the chromosomes (Fig. 3*A*, red), whereas no peak in this range was seen for the cytoplasm (Fig. 3*A*, blue). The 11.3-nm peak in the chromosomes is consistent with previous studies using optical diffraction (23). There was no evidence of a peak in the 20–80 nm range (Fig. 3*B*, red) in the chromosomes. However, the 1-DRAPS of the cytoplasm showed a peak of 30–40 nm (Fig. 3*B*, blue), which may correspond to the dimensions of the globular complexes, which are abundant in the cytoplasm.

The single peak for the ≈11-nm spacing and absence of other peaks in the chromosomes reveal the predominance of an 11-nm structural feature in chromosomes. To understand more clearly

CELL BIOLOGY

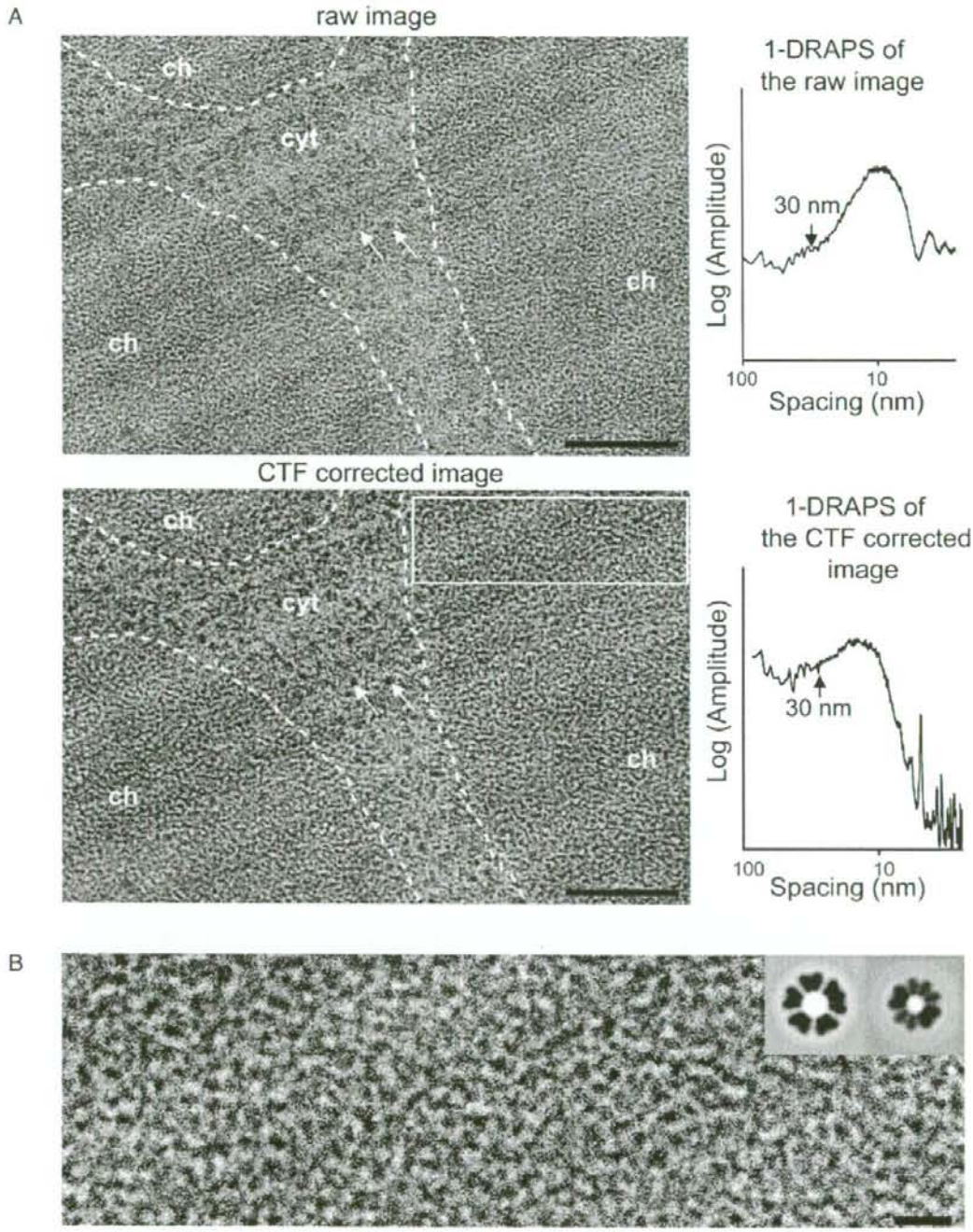


**Fig. 2.** The characteristic grainy texture of the chromosome is maintained after CTF correction. (*A*) An area of a mitotic HeLa S3 cell section that contains 3 parts of chromosomes (outlined in white) separated by the cytoplasm, is shown before and after CTF correction. The corresponding 1-DRAPS shown on the right side. The amplitudes are plotted as arbitrary units by using logarithmic scale on the *y* axis. The *y* axis units are the same in both plots. (*B*) A magnified segment of the CTF-corrected chromosomal texture. The inset in *B* shows simulated top views of 30-nm fibers assembled the interdigitated solenoid (left inset) (22), and 2-start helix (right inset) (27). The simulation was low-pass filtered to make it compatible with the CTF-corrected image of the chromosome. (Scale bars, 200 nm in *A* and 30 nm in *B*.)

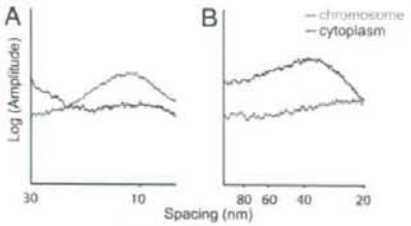


**Fig. 3.** Averaged 1-DRAPS of chromosomes (red) and cytoplasm (blue) after CTF correction reveals characteristic spacing peaks. Two ranges of spacing are shown: from 7 to 30 nm (*A*) and from 20 to 100 nm (*B*). A broad peak of spacing with a maximum of ~11.3 nm is observed for the chromosomes, whereas no peaks within this range are detected for the cytoplasm. In the 20–80 nm range, the chromosomal texture shows no spacing peaks. In contrast, a peak with maximum at ~30 nm is detected in the cytoplasm.

the organization underlying the ≈11-nm peak, we carried out gradual swelling of the mitotic chromatin in vitro.

**Swelling of Chromosomes Reveals That the ~11-nm Spacing Peak Results from the Close-Neighbor Distance Between Nucleosomes.** Isolated metaphase HeLa S3 chromosomes frozen in the presence of 5 mM $Mg^{2+}$ were compact and showed a homogeneous grainy texture (Fig. 4, 5 mM), which was very similar to that observed in mitotic cells (Fig. 2). Consistent with that observed in situ, this texture was characterized by a ≈11-nm spacing peak and by the absence of peaks of large spacing. Decreasing the $Mg^{2+}$ concentration in the incubation buffer resulted in gradual swelling of the chromosomes. At 1.5 mM $Mg^{2+}$, there were no significant global changes in chromosome structure, although the peak spacing was slightly displaced (11.8 nm) (Fig. 4, 1.5 mM). At 0.7 mM $Mg^{2+}$, the mitotic chromosomes were no longer compacted but consisted of irregular chromatin patches extending over regions of ≥100 nm (Fig. 4, 0.7 mM). The peak maximum was further displaced toward the larger dimension (13.7 nm). Lastly, at 0.5 mM $Mg^{2+}$, the chromosome appeared as irregular filaments formed from discrete grains, which were consistent with nucleosomes in terms of their size and shape (Fig. 4, 0.5 mM). These filaments were reminiscent of the irregular 30-nm fibers observed in vitro (21). The peak in the 7–20 nm range persisted in the 1-DRAPS, with the maximum located at ≈14.3 nm. This value is substantially larger than any dimension of nucleosome, which indicates that the peak results from nucleosome spacing. Because no particular order of spatial positioning of nucleosomes was observed within the filaments, the peak reflects a general preferential distance between the centers of neighboring nucleosomes. The gradual shift of the spacing peak with swelling suggests that the peak has the same origin in open fibers and in partially decompacted and fully compacted native chromosomes. Therefore, the compact native chromosome appears to be a chromatin mass in which nucleosomes are packed in no particular order, albeit with a preferential distance of ≈11 nm.

In addition to the 14.3-nm peak, the power spectrum of chromosomes swollen at 0.5 mM $Mg^{2+}$ is characterized by a spacing peak in the range of 40–50 nm (data not shown). It appears that this peak is caused not only by the fiber thickness (≈30 nm), but also by a complicated function of interfibrillar spacing, which shifts this peak to larger distances.

The complete removal of magnesium ions by 1 mM EDTA resulted in further swelling and complete loss of the peak (Fig. 4, 1 mM EDTA). This state resembles the fully open isolated chromatin fibers previously observed in the thin vitrified layer in low-salt buffer (21).

## Discussion

We demonstrate that after CTF correction, the images of human mitotic chromosomes in the vitreous sections reflect a compact

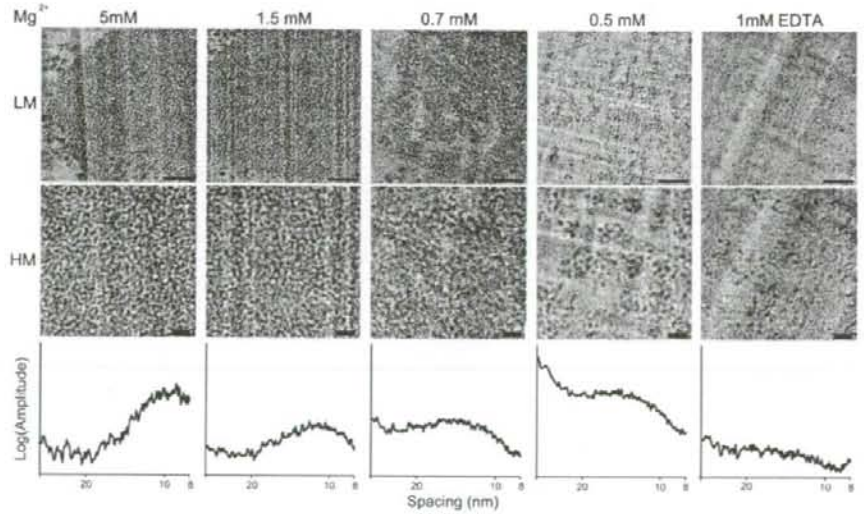


**Fig. 4.** Swelling of isolated mitotic HeLa S3 chromosomes in vitro by decreasing the $Mg^{2+}$ concentration. The vertical columns of the images show the appearance of chromosomes at the corresponding $Mg^{2+}$ concentration in the swelling buffer. Each column contains a cryo-EM image of the vitreous section taken at low magnification (LM), high magnification (HM), and the averaged CTF-corrected 1-DRAPS for the spacing range of 8–30 nm. Note that the texture of isolated chromosome in 5 mM $Mg^{2+}$ is very similar to that of native chromosomes observed in the mitotic cell section (see Fig. 2) and is consistently characterized by a spacing peak with maximum at ~11 nm. Also noteworthy is the gradual shift of this spacing peak that accompanies the gradual swelling of the chromosomes with decreasing $Mg^{2+}$ concentration. Complete removal of $Mg^{2+}$ by EDTA results in fully decompacted chromatin fibers and loss of the spacing peak in the observed range (1 mM EDTA). [Scale bars, 100 nm (LM) and 30 nm (HM).]

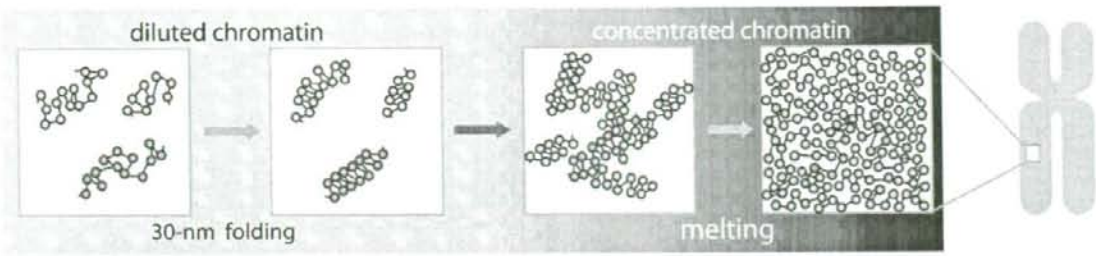


**Fig. 5.** The melt model of mitotic chromosome structure. Under diluted conditions, the flexible nucleosomal fibers may compact through selective close neighbor associations, thus forming the 30-nm chromatin fibers. An increase in chromatin concentration results in interfiber nucleosomal contacts, which interfere with the intrafiber bonds. Nucleosomes of adjacent fibers interdigitate and intermix. The 30-nm folding is disrupted and the nucleosomal fibers melt into a uniform mass. Because there is no difference between the intrafiber and interfiber nucleosome affinities, the nucleosomal filaments return to the open disordered conformation of the diluted state before compaction. Note that the chromatin compaction events are linked to the sequence in the figure to better illustrate the principle of the melt formation. The actual compaction pathway leading to the chromatin melt in vivo is unknown.

uniform chromatin mass, in which 30-nm chromatin fibers are not discernible by visual inspection; 1-DRAPS analysis of the chromosome images also gave no indication of 30-nm chromatin fibers.

The previous cryo-EM observations of starfish spermatozoids or isolated chicken erythrocyte nuclei provided conclusive evidence that 30-nm fibers are maintained after the high-pressure freezing and thin sectioning of vitreous material (25). Therefore, the absence of 30-nm fibers in images of chromosomes is not due to a technical aspect of cryo-EM of vitreous sections, but is characteristic of native HeLa S3 metaphase chromosomes.

This phenomenon can be explained by a model that takes into account internucleosome interactions. The formation of a compact 30-nm fiber requires the selective binding of nucleosomes, which are close neighbors on the DNA strand. For example, if the side-to-side binding of a nucleosome to its first neighbor is stabilized, it will give rise to a 30-nm fiber that is organized as a 1-start helix, a solenoid (26). The second neighbor binding will result in a 2-start helix or a zig-zag ribbon fiber (27). Such selective intrafiber nucleosomal associations can be accomplished under diluted conditions, as in in vitro systems, in which interactions between chromatin fibers or between distant segments of the same nucleosome chain are negligible (Fig. 5, diluted). However, these interactions become common during chromosome compaction in vivo and, thus, interfere with the formation and/or maintenance of selective intrafiber bonds (Fig. 5, concentrated). In this type of situation, 30-nm folding can exist only if the specific intrafiber nucleosomal binding has higher affinity than other internucleosomal associations. In this case, chromosome swelling first disrupts the weaker bonds, leaving the stronger, specific, intrafiber bonds intact. Consequently, the swelling would give rise to segregation of the 30-nm fibers, which remain compacted. However, this scenario is not compatible with our observations. Initially, the chromosome swells as a uniform mass, and then gradually dissociates into chromatin filaments of rather irregular open zig-zag structures, rather than compact 30-nm fibers. Thus, it appears that within the mitotic bulk of chromatin there is no crucial difference between the forces of interfiber and intrafiber nucleosomal associations. A nucleosome interacts with its neighbors irrespective of the nucleosomal array along the DNA strand. This state is known as a "melt" in polymer physics (28). It means that the nucleosome does not "know" to which fiber it belongs. In this case, no global secondary DNA folding exists, and 30-nm fibers, even if they existed before mitosis, would melt into the uniform mass and lose their structural identity (Fig. 5). The concept of the melt implies dynamic polymer chains (28): polymer chains are constantly moving and rearranging at the local level. Given that it is also valid for the mitotic chromatin, the melt model provides conclusive explanations of the 2 following observations, which are difficult to be interpreted by 30-nm-fiber models.

The first is the unexpectedly high intra-chromosome diffusion capabilities of many of the soluble factors (29–33). Of these factors, essential structural components of chromosomes, topoisomerase IIα and condensins, are comparable with or larger than nucleosomes. Accordingly, their diffusion within a static chromatin structure would require a sufficient porosity that is not compatible with the highly-dense metaphase chromatin packing (34, 35). The dynamic melt overcomes this problem: constant local movements and rearrangements of the nucleosomes by Brownian motion allow the protein complexes to enter and to move through the bulk of the chromosome. The previously reported high mobility of linker histone H1 in the metaphase chromosomes, suggesting a transient mode of H1 binding, is in agreement with the dynamic state of the chromatin (29).

Second, the melt state overcomes a packing problem. According to available measurements, the local DNA concentration in mammalian mitotic chromosomes is high at ≈170 mg/mL (34, 35). Typical models of chromosome organization based on 30-nm fibers face difficulties in reaching this value, because even a dense packing of 30-nm fibers unavoidably leaves a significant unoccupied space between the fibers (34, 35). The melt, which is a homogeneous dense packing without any empty space, could avoid this problem.

Because, in addition to human cells, similar disordered homogeneous chromatin has been observed by cryo-EM in not only the mitotic, but also the interphase chromatins of rodents and plant cells, the melt may represent the predominant state of compacted chromatin in vivo in general (36, 37). When 30-nm chromatin folding is required locally (e.g., in specific loci) or globally in the entire chromatin of specific cell types (e.g., in starfish spermatozoids; see ref. 25), transition of the homogeneous melt into 30-nm fibers may be caused in vivo through increasing of intrafiber nucleosome affinity (e.g., by histone modifications or binding of specific proteins). A similar effect may be caused by nonphysiological treatments used in conventional TEM, which may account for the 30-nm fibers observed in plastic-embedded chromosomes (9, 10).

Further refinement of the melt model will address the questions of how the chromosome shape is formed and how the structural integrity of the chromosome is maintained in the highly dynamic chromatin state. These advances will be made possible by improved computer modeling and in vivo molecular dynamic measurements, together with the 3D reconstruction of chromatin by using cryo-electron tomography.

## Materials and Methods

**Preparation of Mitotic Cells and Chromosomes and High-Pressure Freezing.** HeLa S3 cells were grown in RPMI medium 1640 that was supplemented with 10% FBS (Invitrogen). The yield of mitotic cells was increased by adding 0.06 μg/mL colcemide (Sigma-Aldrich) to the culture medium for 4 h. Mitotic cells were collected by shaking and were pelleted by centrifugation at 1000 × *g* for 5 min. The cell pellet was mixed with 5 volumes of culture medium that contained 20% dextran (40 kDa; Sigma-Aldrich). The mixture was placed on a stack of filter papers and incubated for 5 min in a humid chamber. Concentrated suspensions of cells were rapidly collected from the droplet on the filter paper and placed into specimen carriers before freezing under high pressure (HPM 010; BAL-TEC).

Mitotic chromosome clusters were purified as described previously (9). Vitrification of isolated chromosome clusters, as well as entire cells by high-pressure freezing requires the addition of 20% dextran solution to the swelling buffer. Although dextran with molecular mass of 40 kDa gave satisfactory results for cell vitrification, its presence in the swelling buffer prevented the swelling of chromosomes. We found that 1.5-kDa dextran (Sigma-Aldrich) produced optimal chromosome swelling and sectioning.

To swell the chromosomes, chromosome clusters were diluted in 100 volumes of buffer that contained 10 mM Hepes-KOH (pH 7.5), 20% dextran, and $MgCl_2$ at the indicated concentration. The clusters were then pelleted by centrifugation at 8000 × *g* for 5 min, and frozen at high pressure by using the Leica EM-PACT machine.

**Cryo-Sectioning and Cryo-EM.** Frozen cells were sectioned by using the EM UC-6 FC-6 cryomicrotome (Leica) at −140 °C. Vitrified chromosome clusters were cut at −170 °C, because sectioning at a higher temperature resulted in a strong relief on the section surface. Sections with nominal thickness of 40 nm were produced with a 25° or 35° diamond cutting knife (Diatome). Sections were transferred onto lacy carbon-covered 300-mesh copper grids (Agar Scientific). The grids were transferred to a Gatan cryoholder (Gatan) that was maintained at a temperature below −170 °C and then inserted into a precooled CM100 cryo-electron microscope (FEI), which was equipped with a LaB6 cathode with an accelerating voltage of 100 kV. Electron diffraction was used to check whether the water was vitreous or crystalline. Crystalline sections were discarded. Images were recorded with the TemCam-F224HD charge-coupled-device camera (Tietz Video and Image Processing Systems).

**Focal Series Reconstruction and Deconvolution.** Focal series of images of the same area were taken with defocus levels ranging from 6 to 30 μm at 25,000× magnification (0.65 nm per pixel). The images were aligned in Adobe Photoshop 7.0. 1-DRAPS were calculated in SumpS (24) and a Gaussian curve was fitted by using the KaleidaGraph 4.0 software (Synergy Software). The images were denconvoluted and merged in CTFMIX (24). The simulations of topviews of 30-nm fibers were performed in Matlab (The MathWorks). The PDB files of 30-nm fiber models were kindly provided by D. Rhodes.

**Quantitative Image Analysis by 1-DRAPS.** Appropriate digital micrographs of chromatin were selected on the basis of optimal defocus levels and minimal cutting distortions and astigmatism. A magnification level of 25,000× (0.65 nm per pixel) with a defocus range from −5 to −10 μm was used for 1-DRAPS with a spacing of 7–20 nm. For the spacing range of 15–40 nm, several groups of images were collected at 10,000× magnification (1.62 nm per pixel), and the defocus was in the range of 37–60 μm. Chromatin areas were excised from the images into irregular regions or into squares of $512^2$, $1024^2$, or $2048^2$ pixels in Adobe Photoshop 7.0. The total collected ch area was ≈51.7 $\mu m^2$ for the 7–15 nm range of 1-DRAPS and 280 $\mu m^2$ for the 15–40 nm range. Excised images were padded into squares of $4096^2$ pixels, and were orientated so that the knife marks were vertical. Images were masked in Fourier space, by using Image J 1.38a (National Institutes of Health, http://rsb.info.nih.gov/ij/), to remove signals that corresponded to knife marks and crevasses (for further details, see *SI Text* and Fig. S1). We calculated 1-DRAPS for each image by using SumPS (24). CTF correction by deconvolution of individual images was performed by using CTFMIX. Gaussian coefficients were calculated in KaleidaGraph 4.0. All image processing was performed on a Dell Inspiron running Ubuntu 6.06. The averaged deconvoluted 1-DRAPS, which corresponded to individual conditions and cutting conditions, were calculated in CTFMIX and KaleidaGraph 4.0. File format conversion was performed by using EM2EM (Imagic Science).

**ACKNOWLEDGMENTS.** We thank Dr. D. Rhodes (Laboratory of Molecular Biology, Medical Research Council, Cambridge, UK) for providing models of 30-nm fibers, and Drs. A. Stasiak and H. Saibil for their comments. M.E, A.S.F., and J. D. were supported by the 3D-EM Network of Excellence within Research Framework Program 6 of the European Commission. K.M. was supported by a grant-in-aid and the Promotion of X-Ray Free Electron Laser Research of the Ministry of Education, Culture, Sports, Science and Technology, and by a Ministry of Health, Labour, and Welfare grant for Advanced Medical Technology.

1. Becker WM, Reece JB, Poenie MF (1996) in *The World of the Cell*, ed Becker WM (Benjamin-Cummings Publishing Company, Menlo Park, CA), pp 434–435.
2. Kornberg RD (1974) Chromatin structure: A repeating unit of histones and DNA. *Science* 184:868–871.
3. Oudet P, Gross-Bellard M, Chambon P (1975) Electron microscopic and biochemical evidence that chromatin structure is a repeating unit. *Cell* 4:281–300.
4. Kornberg RD, Lorch Y (1999) Twenty-five years of the nucleosome, fundamental particle of the eukaryote chromosome. *Cell* 98:285–294.
5. Swedlow JR, Hirano T (2003) The making of the mitotic chromosome: Modern insights into classical questions. *Mol Cell* 11:557–569.
6. Belmont AS (2006) Mitotic chromosome structure and condensation. *Curr Opin Cell Biol* 18:632–638.
7. Maeshima K, Eltsov M (2007) Packaging the genome: The structure of mitotic chromosomes. *J Biochem* 143:145–153.
8. Gasser SM, Laroche T, Falquet J, Boy de la Tour E, Laemmli UK (1986) Metaphase chromosome structure. Involvement of topoisomerase II. *J Mol Biol* 188:613–629.
9. Marsden MP, Laemmli UK (1979) Metaphase chromosome structure: Evidence for a radial loop model. *Cell* 17:849–858.
10. Maeshima K, Eltsov M, Laemmli UK (2005) Chromosome structure: Improved immunolabeling for electron microscopy. *Chromosoma V* 114:365–375.
11. Belmont A, Sedat J, Agard D (1987) A three-dimensional approach to mitotic chromosome structure: Evidence for a complex hierarchical organization. *J Cell Biol* 105:77–92.
12. Kireeva N, Lakonishok M, Kireev I, Hirano T, Belmont AS (2004) Visualization of early chromosome condensation: A hierarchical folding, axial glue model of chromosome structure. *J Cell Biol* 166:775–785.
13. Poirier MG, Marko JF (2003) Micromechanical studies of mitotic chromosomes. *Curr Top Dev Biol* 55:75–141.
14. Gall JG (1966) Chromosome fibers studied by a spreading technique. *Chromosoma* 20:221–233.
15. Adolph KW (1980) Organization of chromosomes in mitotic HeLa cells. *Exp Cell Res* 125:95–103.
16. Paulson JR, Langmore JP (1983) Low angle x-ray diffraction studies of HeLa metaphase chromosomes: Effects of histone phosphorylation and chromosome isolation procedure. *J Cell Biol* 96:1132–1137.
17. Langmore JP, Paulson JR (1983) Low angle x-ray diffraction studies of chromatin structure in vivo and in isolated nuclei and metaphase chromosomes. *J Cell Biol* 96:1120–1131.
18. Al-Amoudi A, *et al.* (2004) Cryo-electron microscopy of vitreous sections. *EMBO J* 23:3583–3588.
19. Dubochet J, *et al.* (1988) Cryo-electron microscopy of vitrified specimens. *Q Rev Biophys* 21:129–228.
20. Frank J (1996) *Three-Dimensional Electron Microscopy of Macromolecular Assemblies* (Academic, San Diego), pp 34–70.
21. Bednar J, Horowitz RA, Dubochet J, Woodcock CL (1995) Chromatin conformation and salt-induced compaction: Three-dimensional structural information from cryoelectron microscopy. *J Cell Biol* 131:1365–1376.
22. Robinson PJJ, Fairall L, Huynh VAT, Rhodes D (2006) EM measurements define the dimensions of the "30-nm" chromatin fiber: Evidence for a compact, interdigitated structure. *Proc Natl Acad Sci USA* 103:6506–6511.
23. McDowall AW, Smith JM, Dubochet J (1986) Cryo-electron microscopy of vitrified chromosomes in situ. *EMBO J* 5:1395–1402.
24. Conway JF, Steven AC (1999) Methods for reconstructing density maps of "single" particles from cryoelectron micrographs to subnanometer resolution. *J Struct Biol* 128:106–118.
25. Woodcock CL (1994) Chromatin fibers observed in situ in frozen hydrated sections. Native fiber diameter is not correlated with nucleosome repeat length. *J Cell Biol* 125:11–19.
26. Robinson PJ, Rhodes D (2006) Structure of the "30 nm" chromatin fibre: A key role for the linker histone. *Curr Opin Struct Biol* 16:336–343.
27. Dorigo B, *et al.* (2004) Nucleosome arrays reveal the two-start organization of the chromatin fiber. *Science* 306:1571–1573.
28. de Gennes PG (1979) *Scaling Concepts in Polymer Physics* (Cornell Univ Press, Ithaca, NY).
29. Chen D, *et al.* (2005) Condensed mitotic chromatin is accessible to transcription factors and chromatin structural proteins. *J Cell Biol* 168:41–54.
30. Christensen MO, *et al.* (2002) Dynamics of human DNA topoisomerases IIalpha and IIbeta in living cells. *J Cell Biol* 157:31–44.
31. Oliveira RA, Heidmann S, Sunkel CE (2007) Condensin I binds chromatin early in prophase and displays a highly dynamic association with Drosophila mitotic chromosomes. *Chromosoma* 116:259–274.
32. Tavormina PA, *et al.* (2002) Rapid exchange of mammalian topoisomerase II alpha at kinetochores and chromosome arms in mitosis. *J Cell Biol* 158:23–29.
33. Gerlich D, Hirota T, Koch B, Peters JM, Ellenberg J (2006) Condensin I stabilizes chromosomes mechanically through a dynamic interaction in live cells. *Curr Biol* 16:333–344.
34. Daban JR (2000) Physical constraints in the condensation of eukaryotic chromosomes. Local concentration of DNA versus linear packing ratio in higher order chromatin structures. *Biochemistry* 39:3861–3866.
35. Daban JR (2003) High concentration of DNA in condensed chromatin. *Biochem Cell Biol* 81:91–99.
36. Bouchet-Marquis C, Dubochet J, Fakan S (2006) Cryoelectron microscopy of vitrified sections: A new challenge for the analysis of functional nuclear architecture. *Histochem Cell Biol* 125:43–51.
37. Dubochet J, Sartori Blanc N (2001) The cell in absence of aggregation artifacts. *Micron* 32:91–99.

LETTERS

# Heterochromatin links to centromeric protection by recruiting shugoshin

Yuya Yamagishi[1,2], Takeshi Sakuno[1,3], Mari Shimura[4] & Yoshinori Watanabe[1,2]

**The centromere of a chromosome is composed mainly of two domains, a kinetochore assembling core centromere and peri-centromeric heterochromatin regions[1,2]. The crucial role of centromeric heterochromatin is still unknown, because even in simpler unicellular organisms such as the fission yeast *Schizosaccharomyces pombe*, the heterochromatin protein Swi6 (HP1 homologue) has several functions at centromeres, including silencing gene expression and recombination, enriching cohesin, promoting kinetochore assembly, and, ultimately, preventing erroneous microtubule attachment to the kinetochores[1,3–6]. Here we show that the requirement of heterochromatin for mitotic chromosome segregation is largely replaced by forcibly enriching cohesin at centromeres in fission yeast. However, this enrichment of cohesin is not sufficient to replace the meiotic requirement for heterochromatin. We find that the heterochromatin protein Swi6 associates directly with meiosis-specific shugoshin Sgo1, a protector of cohesin at centromeres. A point mutation of Sgo1 (V242E), which abolishes the interaction with Swi6, impairs the centromeric localization and function of Sgo1. The forced centromeric localization of Sgo1 restores proper meiotic chromosome segregation in *swi6Δ* cells. We also show that the direct link between HP1 and shugoshin is conserved in human cells. Taken together, our findings suggest that the recruitment of shugoshin is the important primary role for centromeric heterochromatin in ensuring eukaryotic chromosome segregation.**

To delineate the molecular function of centromeric heterochromatin, we explored whether any mutation of *swi6*$^+$ could separate the two major functions of heterochromatin, transcriptional silencing and chromosome segregation. The null allele of *swi6*$^+$, when combined with tagging of Psc3 (a cohesin subunit) with green fluorescent protein (GFP), results in temperature-sensitive growth[5]. This is presumably because the localization of cohesin at the centromere, which is decreased by *swi6Δ*, is further functionally compromised by the tagging of the cohesin subunit. By mutagenizing the *swi6*$^+$ gene on a background of *psc3–GFP*, we were able to isolate a mutant *swi6-sm1* that showed a defect in transcriptional silencing but not in growth at high temperature (Supplementary Fig. 1). We confirmed that the *swi6-sm1* mutation by itself produces defects in the transcriptional silencing of an integrated marker that localizes in the peri-centromeric regions, like *swi6Δ* (Fig. 1a). By contrast, characteristics potentially related to chromosome segregation (sensitivity to thiabendazole, localization of cohesin at centromeres, chromosome lagging at anaphase, and mini-chromosome maintenance) are all intact in *swi6-sm1* cells, as they are in wild-type cells (Fig. 1a–d). These results indicate that the function of transcriptional silencing is separable from chromosome segregation on the Swi6/HP1 protein.

Together with the previous result that cohesin at centromeres is important for chromosome segregation but not for transcriptional silencing[3,6], the foregoing results indicate that the primary requirement of heterochromatin for mitotic chromosome segregation might be the recruitment of cohesin. To explore this assumption, we sought to localize cohesin at the centromere in a heterochromatin-independent way, and to test its ability to suppress the chromosome segregation defects of heterochromatin-negative cells. For this purpose, we endowed Psc3 with its own ability to localize to the centromere by fusing its carboxy-terminal end with two copies of chromodomain (CD), which binds to H3K9me (histone H3 methylated on Lys 9), which locates mainly in the peri-centromeric

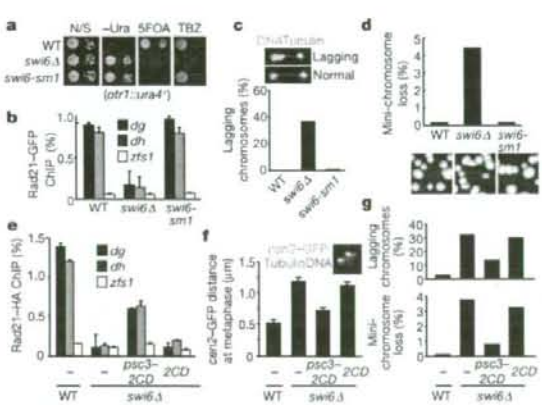


**Figure 1 | Forced enrichment of cohesin in the peri-centromeric regions can substitute for the requirement of heterochromatin for mitotic chromosome segregation. a**, Serial dilutions of the indicated cultures were plated on nonselective (N/S), uracil-lacking (−Ura) or 5-fluoro-orotic acid (5FOA) medium to assay *ura4*$^+$ expression at the outer centromeric repeats. Sensitivity to thiabendazole (TBZ) was assayed similarly. WT, wild type. **b**, The indicated *rad21*$^+$*–GFP* cells were cultured and fixed for ChIP analysis in the peri-centromeric region (*dg* and *dh*) and arm region (*zfs1*). Error bars represent s.d. ($n = 3$). **c**, Frequencies of lagging chromosomes in anaphase cells ($n > 100$) were examined at 18 °C. **d**, Mini-chromosome loss rate per division was assayed in the indicated cells ($n > 1{,}000$). The loss of mini-chromosome results in red colonies as a result of adenine auxotrophy. **e**, Rad21–haemagglutinin (HA) levels were measured in the indicated cells by ChIP analysis. Error bars represent s.d. ($n = 3$). **f**, The indicated cells cultured at 25 °C were shifted to 36 °C for 4 h (metaphase arrest by *cut9-665*), fixed and stained for tubulin. The distance between *cen2*–GFP dots was measured in metaphase (short spindle) cells. Error bars represent s.e.m. ($n = 50$). **g**, Mini-chromosome loss rate per division ($n > 1{,}000$) and frequencies of lagging chromosome at anaphase ($n > 100$) were assayed in the indicated cells.

[1]Laboratory of Chromosome Dynamics, Institute of Molecular and Cellular Biosciences, [2]Graduate Program in Biophysics and Biochemistry, Graduate School of Science, and [3]Promotion of Independence for Young Investigators, University of Tokyo, Yayoi, Tokyo 113-0032, Japan. [4]Department of Intractable Diseases, International Medical Center of Japan, Tokyo 162-8655, Japan.

regions[7]. We confirmed that Psc3–2CD, as well as 2CD, itself localizes at discrete nuclear dots in *swi6Δ* cells, which preserve sufficient H3K9me in the intrinsic heterochromatin regions in spite of the heterochromatin defect, but not in another heterochromatin-defective strain, *clr4Δ*, which lacks H3K9me (ref. 7) (Supplementary Fig. 2a). As predicted, the additional expression of Psc3–2CD (but not of 2CD alone) improved the localization of the cohesin complex to the peri-centromeric regions and also centromeric cohesion in *swi6Δ* cells (Fig. 1e, f). We confirmed that the expression of Psc3–2CD does not restore transcriptional silencing in *swi6Δ* cells (Supplementary Fig. 3a). To explore the impact of cohesion recovery on the defective chromosome segregation in *swi6Δ* cells, we used a mini-chromosome loss assay. The fidelity of chromosome segregation was largely restored by the expression of Psc3–2CD but not that of 2CD (Fig. 1g). Consistently, the frequency of lagging chromosomes in anaphase reduced in *swi6Δ Psc3–2CD* cells but not in *swi6Δ 2CD* cells (Fig. 1g). These results unequivocally validate the previously expected, but not proven, notion that the primary requirement of heterochromatin for mitotic chromosome segregation is the enrichment of cohesin at the centromere[5,6].

In meiotic chromosome segregation, monopolar attachment of sister kinetochores to the spindle is established in metaphase I; sister chromatids therefore move together to the same side of the zygote (reductional division) in the following anaphase I. During meiosis I, meiosis-specific shugoshin Sgo1 and its partner, protein phosphatase 2A (PP2A), protect the centromeric cohesin from separase cleavage. Bipolar attachment at the following meiosis II is therefore secured by the residual cohesion at the centromere[8–11] (Fig. 2a). As with *sgo1Δ* cells, *swi6Δ* cells undergo intact meiosis I but suffer a nondisjunction of sister chromatids in meiosis II (refs 8, 12) (Fig. 2a, b). This can be explained by the fact that meiotic prophase *swi6Δ* cells have a decrease in the primary enrichment of cohesin (including Rec8–Psc3) to 30–40% in peri-centromeric regions[12], which should be protected by Sgo1 in the following anaphase I. The transcriptional silencing of Swi6 is not relevant to this function, because *swi6-sm1* cells have intact meiotic chromosome segregation (Supplementary Fig. 4). We therefore assumed that the forced localization of cohesin at the centromere would also restore the meiotic defects of *swi6Δ* cells. However, the expression of Psc3–2CD scarcely restored the *swi6Δ* defect in meiosis II (data not shown; see also Fig. 2g). This result indicates that the primary requirement of heterochromatin for meiotic chromosome segregation may be something other than cohesin enrichment.

In a search, involving a yeast two-hybrid assay, for proteins that interact with Sgo1, we frequently isolated Swi6. This interaction was confirmed by co-immunoprecipitation in extracts of fission yeast (Fig. 2c). Consistent with the fact that these proteins become enriched in the peri-centromeric regions[8], Sgo1 and Swi6 largely co-localized in the cells at metaphase I (Fig. 2d). These results, together with the above assumption, prompted us to link Swi6 to the Sgo1 function. Accordingly, the measurement of fluorescence intensity of centromeric Sgo1–GFP in metaphase I-arrested cells revealed that Sgo1 localization is impaired in *swi6Δ* cells (Fig. 2e), although meiotic expression of Sgo1 protein was not affected by *swi6Δ* (Supplementary Fig. 5). These results indicate that Swi6 is crucial in localizing Sgo1 and thereby promotes the protection of cohesin from separase during anaphase I. To determine whether Sgo1 localization is the primary meiotic target of Swi6, we fused Sgo1 with CD to localize Sgo1 at centromeres in a heterochromatin-independent way and examined its ability to suppress meiotic defects in *swi6Δ* cells. Sgo1–CD did indeed localize at the centromere regardless of *swi6Δ* (Fig. 2f). The expression of Sgo1–CD in place of endogenous Sgo1 mostly suppressed nondisjunction during meiosis II in *swi6Δ* cells (Fig. 2g; compare the *2CD sgo1*$^{+}$ and *2CD sgo1–CD* columns). This suppression requires the amino-terminal coiled-coil domain of Sgo1, a region that associates with PP2A (see below), which is indicative of the specificity of the suppression (Supplementary Fig. 6). Moreover, the suppression became nearly complete when Psc3–2CD was co-expressed (Fig. 2g; compare the rightmost two columns). These results indicate strongly that the centromeric recruitment of Sgo1 is the primary role for heterochromatin in meiotic chromosome segregation, although the enrichment of cohesin also contributes to ensure that sufficient cohesin is protected by Sgo1 until meiosis II. The defect in disjunction at meiosis II is partial in *swi6Δ* cells in comparison with *sgo1Δ* cells (Fig. 2b), and residual centromeric signals of Sgo1 are detectable in *swi6Δ* cells (Fig. 2e), indicating the possible existence of an additional Swi6-independent pathway for centromeric Sgo1 localization (also see Supplementary Fig. 7).

To delineate the interaction of Swi6 and Sgo1, we made several truncations of these proteins and examined their interaction by two-hybrid assay. We found that the interaction depends on the chromoshadow domain (CSD) of Swi6 and a conserved amino-acid residue Phe 324 within it that is known to mediate an interaction with a specific pentapeptide sequence (P/L)xVx(M/I/L/V)[13] (Fig. 3a). In

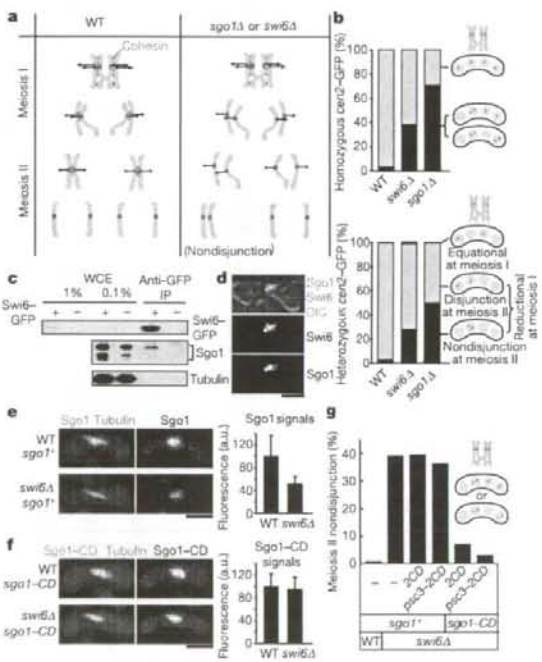


**Figure 2 | Requirement of heterochromatin protein Swi6 for meiosis is replaced by forced localization of Sgo1 at the centromere. a**, Schematic drawing of the behaviour of homologous chromosomes during meiosis. The location of cohesin (red oval) is indicated. WT, wild type. **b**, Both (top) or one (bottom) of the homologues marked with *cen2*–GFP were monitored for segregation during meiosis in the indicated zygotes ($n > 100$). **c**, Whole-cell extracts (WCE) were prepared from proliferating *swi6*$^{+}$*–GFP* or non-tagged cells ectopically expressing Sgo1 and immunoprecipitated (IP) with anti-GFP antibody. The precipitates were examined by western blotting with anti-Sgo1 antibody. The lower bands of Sgo1 represent the degradation products. **d**, Swi6–tdTomato and Sgo1–GFP expressed from endogenous promoters were detected in meiosis I. **e**, Sgo1–GFP signals at metaphase I were measured and compared between wild-type and *swi6Δ* cells. The spindles were visualized by expressing mCherry–Atb2. Error bars represent s.d. ($n = 30$). **f**, Sgo1–GFP–CD signals were measured and compared between wild-type and *swi6Δ* cells. Error bars represent s.d. ($n = 30$). Scale bars, 5 μm. **g**, Both homologues marked with *cen2*–GFP in the indicated zygotes were monitored for segregation during meiosis ($n > 100$). The frequency of zygotes undergoing nondisjunction in either or both meiosis II divisions is shown.

contrast, the Sgo1 peptide responsible for the interaction was limited to 26 residues (222–247), including VCVCI (240–244), which is similar to the CSD-binding motif (Fig. 3b). Accordingly, the replacement of Val 242 with Glu (VE) in Sgo1 abolished the interaction with Swi6 while preserving the interaction with Par1, a subunit of PP2A. An immunoprecipitation assay also supports the loss of the interaction of Sgo1-VE with Swi6 (Fig. 3c). To explore the impact of the loss of the interaction *in vivo*, we expressed *sgo1-VE* from the endogenous promoter and examined the localization of Sgo1. Immunofluorescence assays indicate that the centromeric localization of Sgo1-VE is significantly decreased in comparison with wild-type Sgo1 (Fig. 3d). To delineate the loss of localization more precisely, we performed a chromatin immunoprecipitation (ChIP) assay. The results indicate that Sgo1-VE largely loses the ability to localize in the peri-centromeric region, although Swi6 localization is invariant in this mutant (Fig. 3e). These data indicate that the interaction between Swi6 and Sgo1 is important for Sgo1 localization at centromeres and that Sgo1 acts downstream of heterochromatin assembly at centromeres. The assay of chromosome segregation further revealed that *sgo1-VE* cells provoke nondisjunction in meiosis II, similarly to *swi6Δ* cells (Fig. 3f). The Sgo1-VE protein, when fused with CD and thereby localized to the centromere, can perform its full function in protecting Rec8 (Fig. 3f and Supplementary Fig. 8). These results indicate that Sgo1-VE is solely deficient in the ability to localize at centromeres. Likewise, *sgo1-VE–CD* suppresses *swi6Δ* defects to a similar extent to that of wild-type *sgo1–CD* (Fig. 3f). We noticed that a slightly greater defect is observed in *swi6Δ* cells than in *sgo1-VE* cells, and this is also true in *swi6Δ sgo1-VE–CD* cells compared with *sgo1-VE–CD* cells. This can be accounted for by the difference in the primary localization of cohesin, which is decreased in *swi6Δ* cells[12] but is intact even in *sgo1Δ* cells[9]. Taken together, these results highlight the importance of Val 242 in Sgo1 for Swi6-mediated centromeric localization and the requirement of this interaction for the protection of centromeric cohesin throughout meiosis I division.

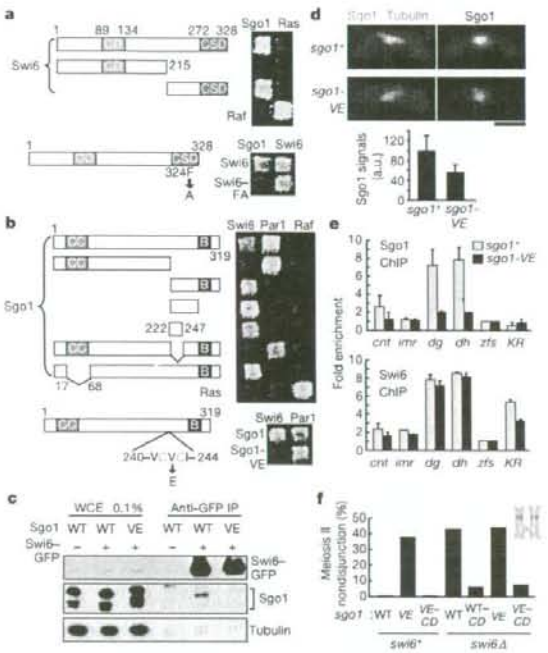


**Figure 3 | Association of Swi6 with Sgo1 is required for the centromeric localization and function of Sgo1.** **a**, Yeast two-hybrid assay indicates that Swi6 interacts with Sgo1 through the CSD. The pair of Ras and Raf acts as positive control. The point mutation F324A (FA) in the CSD abolishes the interaction with Sgo1, while preserving the ability to dimerize. The transformants were grown on plates lacking histidine. **b**, Yeast two-hybrid assay with Sgo1 deletions. Sgo1 interacts with Par1 through the coiled-coil region (CC), and the interaction with Swi6 takes place through the upstream region (222–247 residues) of the conserved basic region (B). A point mutation, V242E (VE), in this region abolishes the interaction. **c**, Whole-cell extracts (WCE) were prepared from mitotic cells ectopically expressing wild-type (WT) Sgo1 or Sgo1-VE protein. Swi6–GFP was immunoprecipitated (IP) with anti-GFP antibody to test for precipitation together with Sgo1. **d**, Sgo1–GFP and Sgo1-VE–GFP were detected at metaphase I and their signals were measured. Error bars represent s.d. ($n = 30$). Scale bar, 5 μm. **e**, A ChIP assay was used to measure Sgo1 (top) and Swi6 (bottom) levels throughout the indicated chromosomal sites (*cnt* and *imr* locate at the core centromere and *KR* at the silent mating-type loci) in cells arrested at metaphase I. Fold enrichment to the arm region (*zfs*) is shown. Error bars represent s.d. ($n = 2$). **f**, Both homologues marked with *cen2*–GFP in the indicated cells were monitored for segregation during meiosis ($n > 100$). The frequency of zygotes undergoing nondisjunction in either or both meiosis II divisions is shown.

Although the protective function of shugoshin is limited in meiosis in yeast (no shugoshin has a function in cohesin protection in mitosis[14]), metazoan shugoshin protects cohesin from the prophase dissociation pathway[15–17], which is accompanied by extensive chromosome condensation and the resolution of chromosomes during mitosis. We then examined whether the link between heterochromatin protein HP1 and shugoshin-dependent centromeric protection is evolutionarily conserved. In mammalian cells, HP1α is the major isoform of HP1; it localizes in the peri-centromeric region[18,19]. Immunoprecipitation with a chromatin extract from mitotic 293T cells indicates that hSgo1 precipitates together with HP1α as well as PP2A (Fig. 4a). Moreover, two-hybrid assays suggest that hSgo1 potentially interacts with all HP1 isoforms through the CSD (Supplementary Fig. 9) and that, at least, the interaction of HP1α is mediated by the conserved residue Trp 174 within the CSD (Fig. 4b). In contrast, the deletions of hSgo1 suggest that the amino-acid residues required for the interaction are located between positions 451 and 456 (PVVKIR), which contains a putative CSD binding motif[13], and the replacement of Val 453 with Glu (hSgo1-VE) results in the loss of the interaction with HP1α (Fig. 4c). Thus, the manner of interaction between HP1α and hSgo1 is highly conserved with that of Swi6 and Sgo1 in fission yeast.

In mammals, HP1 associating at centromeric heterochromatin is largely displaced at mitosis, but a small population remains at centromeres[18,20,21] (Fig. 4d). Immunofluorescence of enhanced GFP (EGFP)-tagged HP1α expressed in HeLa cells clearly gives a signal at the inner centromere[22], co-localizing with hSgo1 (Supplementary Fig. 10). To examine the requirement of HP1 for hSgo1 localization, we treated HeLa cells with short interfering RNA (siRNA) against HP1α. Cell proliferation was obviously delayed in the HP1α siRNA-treated cells, although the mitotic defect was not obvious in unperturbed mitosis (data not shown). However, if the cells were arrested at prometaphase by the addition of nocodazole, hSgo1 localization was abolished in a subpopulation of HP1α siRNA-treated cells but not in control cells (Fig. 4e). Accordingly, the centromeric cohesion was largely dissociated in the hSgo1-lacking chromosomes but not in chromosomes containing hSgo1 (Fig. 4f, magnified panels in the HP1α siRNA-treated spread). The imperfect penetrance of the phenotype can be accounted for in part by the difference in duration of mitotic arrest between cells; spreads with less condensed chromosomes all showed normal localization of hSgo1 even in HP1α siRNA-treated cells (Fig. 4f). Although previous assays in vertebrate cells suggested that the heterochromatin structure at the centromere is required for cohesin retention at metaphase[23,24], our current results suggest that this may be mediated through shugoshin localization. Considering the report that the H3K9me pathway is dispensable for centromeric protection in mouse fibroblasts[25], HP1α responsible for hSgo1 localization might use the hinge domain of HP1α for

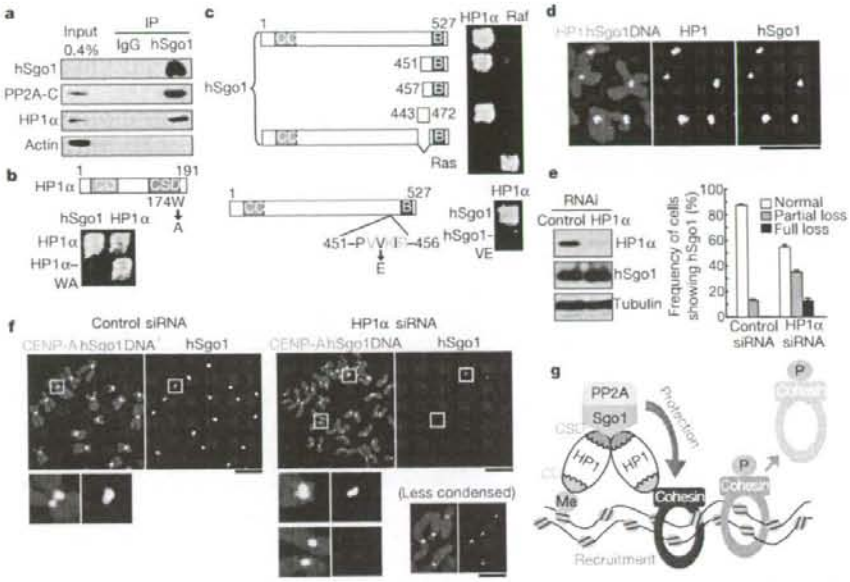


**Figure 4 | The human heterochromatin protein HP1α interacts with human Sgo1 (hSgo1) and is required for its maintenance at centromeres in mitotic chromosomes. a**, A chromatin extract of nocodazole-arrested 293T cells was immunoprecipitated (IP) and analysed by western blotting. **b**, A yeast two-hybrid assay indicating that HP1α interacts with hSgo1 through Trp 174 within the CSD. **c**, Yeast two-hybrid assay using hSgo1 deletions and point mutation. **d**, Spread chromosomes of HeLa cells were immunostained for hSgo1, HP1 and DNA. **e**, HeLa cells treated with control or HP1α siRNA were cultured for 48 h and for a further 4 h after the addition of nocodazole. Depletion of HP1α was examined by western blotting. Spread chromosomes were immunostained for CENP-A, hSgo1 and DNA. Spreads ($n > 50$) were classified according to hSgo1 staining patterns into normal, partial loss (more than 30% hSgo1-negative chromosomes per cell) or full loss. Error bars represent s.d. ($n = 3$). **f**, Representative spreads assayed in **e** are shown magnified in the bottom panel. A spread of an HP1α siRNA-treated cell with less-condensed chromosomes is also shown at the bottom right. Scale bars, 5 μm. **g**, A schematic model illustrating how Swi6/HP1 protects centromeric cohesion.

centromeric retention[19] rather than the CD–H3K9me interaction that is disrupted at mitosis[20,21]. Taken together, our data suggest that HP1 has a pivotal function in localizing and/or maintaining hSgo1 at centromeres through their direct association in mammalian cells as in fission yeast (Fig. 4g).

Accumulating evidence suggests that the heterochromatin protein Swi6/HP1 functions in recruiting several cellular 'effector' proteins to a specific chromatin site and thereby in regulating various chromosomal processes[1]. Given that almost all eukaryotic chromosomes carry heterochromatin in the peri-centromeric regions, Swi6/HP1 may constitute a crucial basis for centromere function. Indeed, recent studies suggest that heterochromatin influences the process of kinetochore establishment at the centromere[4,26,27]. Here we have addressed the primary requirement of heterochromatin for mitotic and meiotic chromosome segregation in a simple unicellular organism, fission yeast. Although the enrichment of cohesin in peri-centromeric regions is an important requirement of heterochromatin in ensuring mitotic chromosome segregation, our analysis reveals that the most crucial requirement during meiosis is the recruitment and/or maintenance of shugoshin at centromeres. Moreover, our analysis demonstrates that the mechanism by which the heterochromatin protein promotes shugoshin-mediated centromeric protection is conserved in human cells. Thus, shugoshin recruitment might be a hitherto unknown primary role for centromeric heterochromatin in eukaryotic chromosomes.

## METHODS SUMMARY

All *Schizosaccharomyces pombe* strains used in this study are listed in Supplementary Table 1. Deletion and tagging of endogenous *sgo1*$^+$, *swi6*$^+$, *rec8*$^+$ and *rad21*$^+$ by GFP, mCherry or tdTomato were performed with the PCR-based gene targeting method for *S. pombe*. To quantify the centromeric fluorescent signals, in-focus images of Sgo1–GFP cells were taken with MetaMorph imaging software (Universal Imaging). We measured the maximum intensity of centromeric signals within cells and subtracted the average of background intensity in the nuclei. A ChIP assay was conducted as described previously[4]. A mini-chromosome loss assay was performed as described previously[3], by culturing cells carrying mini-chromosome Ch16 in medium lacking adenine and plating them onto adenine-limiting plates at 30 °C. Immunoprecipitation was conducted essentially as described previously[14]. Immunofluorescence staining of the spread chromosome of HeLa cells was performed as described[28], using primary antibodies against hSgo1 (1:1,000 dilution) and HP1 (1:100 dilution; Santa Cruz Biotechnology, Inc.) or CENP-A (1:100 dilution; Abcam), which were diluted with buffer A containing 10% goat serum or 0.1% BSA, and secondary antibodies: Alexa Fluor 488 anti-rabbit IgG (1:400 dilution; Molecular Probes, Inc.) and Alexa Fluor 546 anti-rabbit IgG (1:400 dilution; Molecular Probes, Inc.), or Alexa Fluor 546 anti-goat IgG (1:1,000 dilution; Molecular Probes, Inc.) and Alexa Fluor 488 anti-rabbit IgG (1:400 dilution; Molecular Probes, Inc.).

**Full Methods** and any associated references are available in the online version of the paper at www.nature.com/nature.

**Received 8 April; accepted 27 June 2008.**
**Published online 17 August 2008.**

1. Pidoux, A. L. & Allshire, R. C. The role of heterochromatin in centromere function. *Phil. Trans. R. Soc. B* **360**, 569–579 (2005).
2. Amor, D. J., Kalitsis, P., Sumer, H. & Choo, K. H. A. Building the centromere: from foundation proteins to 3D organization. *Trends Cell Biol.* **14**, 359–368 (2004).
3. Grewal, S. I. & Jia, S. Heterochromatin revisited. *Nature Rev. Genet.* **8**, 35–46 (2007).
4. Folco, H. D., Pidoux, A. L., Urano, T. & Allshire, R. C. Heterochromatin and RNAi are required to establish CENP-A chromatin at centromeres. *Science* **319**, 94–97 (2008).
5. Nonaka, N. *et al.* Recruitment of cohesin to heterochromatic regions by Swi6/HP1 in fission yeast. *Nature Cell Biol.* **4**, 89–93 (2002).
6. Bernard, P. *et al.* Requirement of heterochromatin for cohesion at centromeres. *Science* **294**, 2539–2542 (2001).

7. Nakayama, J., Rice, J. C., Strahl, B. D., Allis, C. D. & Grewal, S. I. Role of histone H3 lysine 9 methylation in epigenetic control of heterochromatin assembly. *Science* **292**, 110–113 (2001).
8. Kitajima, T. S., Kawashima, S. A. & Watanabe, Y. The conserved kinetochore protein shugoshin protects centromeric cohesion during meiosis. *Nature* **427**, 510–517 (2004).
9. Rabitsch, K. P. *et al.* Two fission yeast homologs of *Drosophila* Mei-S332 are required for chromosome segregation during meiosis I and II. *Curr. Biol.* **14**, 287–301 (2004).
10. Kitajima, T. S. *et al.* Shugoshin collaborates with protein phosphatase 2A to protect cohesin. *Nature* **441**, 46–52 (2006).
11. Riedel, C. G. *et al.* Protein phosphatase 2A protects centromeric sister chromatid cohesion during meiosis I. *Nature* **441**, 53–61 (2006).
12. Kitajima, T. S., Yokobayashi, S., Yamamoto, M. & Watanabe, Y. Distinct cohesin complexes organize meiotic chromosome domains. *Science* **300**, 1152–1155 (2003).
13. Smothers, J. F. & Henikoff, S. The HP1 chromo shadow domain binds a consensus peptide pentamer. *Curr. Biol.* **10**, 27–30 (2000).
14. Kawashima, S. A. *et al.* Shugoshin enables tension-generating attachment of kinetochores by loading Aurora to centromeres. *Genes Dev.* **21**, 420–435 (2007).
15. Salic, A., Waters, J. C. & Mitchison, T. J. Vertebrate shugoshin links sister centromere cohesion and kinetochore microtubule stability in mitosis. *Cell* **118**, 567–578 (2004).
16. McGuinness, B. E., Hirota, T., Kudo, N. R., Peters, J.-M. & Nasmyth, K. Shugoshin prevents dissociation of cohesin from centromeres during mitosis in vertebrate cells. *PLoS Biol.* **3**, e86 (2005).
17. Kitajima, T. S., Hauf, S., Ohsugi, M., Yamamoto, T. & Watanabe, Y. Human Bub1 defines the persistent cohesion site along the mitotic chromosome by affecting shugoshin localization. *Curr. Biol.* **15**, 353–359 (2005).
18. Minc, E., Allory, Y., Worman, H. J., Courvalin, J. C. & Buendia, B. Localization and phosphorylation of HP1 proteins during the cell cycle in mammalian cells. *Chromosoma* **108**, 220–234 (1999).
19. Hayakawa, T., Haraguchi, T., Masumoto, H. & Hiraoka, Y. Cell cycle behavior of human HP1 subtypes: distinct molecular domains of HP1 are required for their centromeric localization during interphase and metaphase. *J. Cell Sci.* **116**, 3327–3338 (2003).
20. Fischle, W. *et al.* Regulation of HP1-chromatin binding by histone H3 methylation and phosphorylation. *Nature* **438**, 1116–1122 (2005).
21. Hirota, T., Lipp, J. J., Toh, B. H. & Peters, J. M. Histone H3 serine 10 phosphorylation by Aurora B causes HP1 dissociation from heterochromatin. *Nature* **438**, 1176–1180 (2005).
22. Sugimoto, K., Tasaka, H. & Dotsu, M. Molecular behavior in living mitotic cells of human centromere heterochromatin protein HP1α ectopically expressed as a fusion to red fluorescent protein. *Cell Struct. Funct.* **26**, 705–718 (2001).
23. Fukagawa, T. *et al.* Dicer is essential for formation of the heterochromatin structure in vertebrate cells. *Nature Cell Biol.* **6**, 784–791 (2004).
24. Guenatri, M., Bailly, D., Maison, C. & Almouzni, G. Mouse centric and pericentric satellite repeats form distinct functional heterochromatin. *J. Cell Biol.* **166**, 493–505 (2004).
25. Koch, B., Kueng, S., Ruckenbauer, C., Wendt, K. S. & Peters, J. M. The Suv39h-HP1 histone methylation pathway is dispensable for enrichment and protection of cohesin at centromeres in mammalian cells. *Chromosoma* **117**, 199–210 (2008).
26. Obuse, C. *et al.* A conserved Mis12 centromere complex is linked to heterochromatic HP1 and outer kinetochore protein Zwint-1. *Nature Cell Biol.* **6**, 1135–1141 (2004).
27. Okada, T. *et al.* CENP-B controls centromere formation depending on the chromatin context. *Cell* **131**, 1287–1300 (2007).
28. Toyoda, Y. & Yanagida, M. Coordinated requirements of human topo II and cohesin for metaphase centromere alignment under Mad2-dependent spindle checkpoint surveillance. *Mol. Biol. Cell* **17**, 2287–2302 (2006).


**Supplementary Information** is linked to the online version of the paper at www.nature.com/nature.

**Acknowledgements** We thank S. Hauf for reading the manuscript critically; R. Allshire, S. Grewal and the Yeast Genetic Resource Center (YGRC) for yeast strains; J.-i. Nakayama for Swi6 antibody; and all the members of our laboratory for their valuable support and discussion. This work was supported in part by the Global COE programme (Integrative life Science Based on the Study of Biosignaling Mechanisms), MEXT, Japan, the Toray Science Foundation (to Y.W.), Special Coordination Funds for Promoting Science and Technology (to T.S.) and Grants-in-Aid for Research on Advanced Medical Technology, Ministry of Health, Labour and Welfare (to M.S.) and for Specially Promoted Research, MEXT, Japan (to Y.W.).

**Author Contributions** Experiments in Fig. 1 were performed mainly by T.S., those in Figs 2, 3 and 4a–c by Y.Y., and those in Fig. 4d–f by M.S. Experimental design and interpretation of data were conducted by all authors. Y.W. planned the project and wrote the paper with input from co-authors.

**Author Information** Reprints and permissions information is available at www.nature.com/reprints. Correspondence and requests for materials should be addressed to Y.W. (ywatanab@iam.u-tokyo.ac.jp).

## METHODS

***Schizosaccharomyces pombe* strains.** *sgo1*$^{+}$*–flag–GFP* was created as described previously[8]. *sgo1*$^{+}$*–flag–GFP–CD* was created by inserting the CD of Swi6 (residues 69–143) into the C terminus of *sgo1*$^{+}$*–flag–GFP* at an endogenous *sgo1*$^{+}$ locus using a PCR-based gene targeting method. We abbreviate Sgo1–Flag–GFP as Sgo1–GFP or simply Sgo1, and Sgo1–Flag–GFP–CD as Sgo1–GFP–CD or Sgo1–CD. To express Psc3–CFP–2CD, a sequence encoding cyan fluorescent protein (CFP) and two copies of the CD of Chp1 (residues 1–97) were fused to the C terminus of Psc3 and cloned under the promoter P*adh41* (a weak version of the *adh1*$^{+}$ promoter). The resulting plasmid was linearized and integrated at the *lys1*$^{+}$ locus of chromosome I by using the *nat*$^{r}$ marker; Psc3–CFP–2CD was thereby expressed in addition to the endogenous Psc3. To express Sgo1(CCΔ)–Flag–GFP–CD, a sequence of Sgo1–Flag–GFP–CD with the endogenous promoter of *sgo1*$^{+}$ was cloned. Then the sequence corresponding to residues 18–67 of Sgo1 was deleted by using a PCR-based method. The resulting plasmid was linearized and integrated at the locus adjacent to the *zfs1*$^{+}$ gene of chromosome II (we refer to this as the *z* locus) using the *hyg*$^{r}$ marker. To express mCherry–Atb2, a sequence encoding mCherry was fused to the N terminus of *atb2*$^{+}$, cloned under the promoter P*adh15* (a weak version of the *adh1*$^{+}$ promoter), and integrated into the *z* locus. To overexpress Sgo1 in mitotic cells, the endogenous *sgo1*$^{+}$ promoter was replaced with the *nmt1*$^{+}$ promoter or Sgo1 was expressed by the pREP1(*nmt1*$^{+}$ promoter)-*sgo1*$^{+}$ plasmid. To decrease anaphase-promoting complex activity during meiosis, and thereby arrest meiosis at metaphase I, we replaced the promoters of *slp1*$^{+}$ and *cut23*$^{+}$ with that of *rad21*$^{+}$, which is repressed during meiosis[8].

**Two-hybrid assay.** The constructs of *sgo1*, *swi6* and *HP1* derivatives were amplified by PCR, cloned into pBTM116 vectors and used as bait. The constructs of *swi6*, *par1*, *HP1* and *hSGO1* derivatives were amplified by PCR, cloned into pActII, pVP16 or pGADT7 vectors and used as prey. These plasmids were transformed into the L40 strain of *Saccharomyces cerevisiae*. Plates lacking histidine were used as a selective medium.

**Immunoprecipitation from fission yeast extracts.** Cultured cells were harvested, washed with HB buffer (25 mM MOPS pH 7.2, 15 mM $MgCl_2$, 15 mM EGTA, 60 mM β-glycerophosphate, 0.1 mM sodium orthovanadate, 0.1 mM NaF, 15 mM *p*-nitrophenylphosphate, 1% Triton-X100, 1 mM dithiothreitol, 1 mM phenylmethylsulphonyl fluoride and Complete protease inhibitor (Roche)) and disrupted with a Multi-bead shocker (Yasui Kikai); the supernatants were collected after centrifugation. Cell extracts were incubated with anti-GFP polyclonal antibodies (Living Colours Full-length A.v. Polyclonal Antibody; BD Biosciences) for 1 h at 4 °C. Protein A beads (Amersham) were added and incubation was continued for 2 h at 4 °C. After washing the precipitates with HB buffer, we analysed them by SDS–PAGE and western blotting with anti-GFP (1:1,000 dilution; Roche), anti-Sgo1 (ref. 8) (1:1,000 dilution) and TAT1 (1:5,000 dilution) antibodies.

**ChIP assay.** The anti-GFP polyclonal antibody (BD Biosciences) and anti-Swi6 polyclonal antibody were used for immunoprecipitation. DNA prepared from whole-cell extracts or immunoprecipitated fractions was analysed by quantitative PCR with the ABI PRISM 7000 system (Applied Biosystems) with SYBR Premix Ex Taq (Perfect Real Time; Takara). The primers used for PCR were all described previously[8,14]. We included an untagged strain to account for non-specific binding in the ChIP fractions. The immunoprecipitation ratios in each region were divided by that of the *zfs1* region (arm region), giving the enrichment scores.

**Immunoprecipitation from human cell extracts.** 293T cells were harvested after treatment with 330 nM nocodazole for 12 h and were lysed by freezing and thawing. Insoluble materials were collected and chromatin proteins were solubilized by treatment with micrococcal nuclease. The cleared chromatin extract was incubated for 3 h at 4 °C with anti-hSgo1 or rabbit IgG coupled to protein A beads. After washing the beads, we analysed the immunoprecipitates by western blotting with anti-hSgo1 (ref. 17) (1:1,000 dilution), anti-PP2A-C (1:1,000 dilution; BD Biosciences), anti-HP1α (1:1,000 dilution; Chemicon) and anti-actin (1:1,000 dilution; Santa Cruz Biotechnology, Inc).

**Treatment of HeLa cells with siRNA and immunofluorescence labelling of spread chromosomes.** siRNA (200 nM) was used for transfection. The sequences of siRNA for HP1α were previously reported[26] (we obtained essentially the same result with a different siRNA, namely 5′-GGGAGAAGUCA GAAAGUAATT-3′). We treated the siRNA 5′-UAAGGCUAUGAAGAG AUAC-3′ (siCONTROL Non-targeting siRNA no. 2; Dharmacon) as control siRNA. After treatment with siRNAs, HeLa cells were cultured for 48 h and treated with nocodazole (0.1 μg $ml^{-1}$) for 4 h. The rounded-up cells at mitotic phase were collected and gently resuspended in 75 mM KCl and incubated for 10 min at room temperature (20–25 °C). These hypotonically treated cells were sedimented onto slides by cytocentrifugation (Cytospin 4; ThermoShandon) at 600 r.p.m. (41*g*) for 5 min. The area around the spreads was marked with PAP-PEN (Zymed Laboratories, Inc.) and washed with buffer A (10 mM Tris-HCl pH 8.0, 120 mM NaCl, 0.5 mM EDTA, 0.1% Triton X-100) for at least 10 min. The slides were then incubated for 1 h at room temperature in a humid chamber with primary antibodies. After gentle washing three times with buffer A (once for 1 min, twice for 5 min), the slides were further incubated with secondary antibodies for 30 min at room temperature in a humid chamber, and gently washed again three times with buffer A. The cells were then fixed with 4% paraformaldehyde in buffer A for 15 min at room temperature. After gentle washing in PBS-EGTA and staining with 4,6-diamidino-2-phenylindole, the slides were mounted in Vectashield for immunofluorescence microscopy.

**Immunostaining of HeLa cells expressing EGFP-tagged HP1α.** Immunofluorescence staining of human cells was performed as described[29]. The sequence of HP1α was cloned into the pEGFP-C1 vector (Clontech), and the resulting pEGFP-C1-HP1α plasmid was transfected into HeLa cells with the use of FuGENE6 reagent (Roche). HeLa cells expressing EGFP–HP1α were spun onto glass slides with a Cytospin cytocentrifuge (Thermo Electron Corporation) and immunostained with anti-hSgo1 (1:1,000 dilution), anti-GFP (1:1,000 dilution; Molecular Probes), and anti-centromere antibody (1:100 dilution; MBL). Secondary antibodies were Alexa Fluor 488 anti-rabbit antibodies (1:1,000 dilution; Molecular Probes), Alexa Fluor 568 anti-mouse antibodies (1:1,000 dilution; Molecular Probes) and Alexa Fluor 647 anti-human antibodies (1:1,000 dilution; Molecular Probes). Images were captured by DeltaVision SoftWorx software (Applied Precision) and processed by deconvolution and *Z*-stack projection.

29. Lee, J. *et al.* Unified mode of centromeric protection by shugoshin in mammalian oocytes and somatic cells. *Nature Cell Biol.* 10, 42–52 (2008).